Journal of Thermal Science Vol.31, No.6 (2022) 1939–1947

https://doi.org/10.1007/s11630-022-1633-6 **Article ID: 1003-2169(2022)06-1939-09**

Distribution Characteristics of Transmitted Diffuse Solar Radiation on the Indoor Surface

YAO Wanxiang[1,2*], TIAN Wanfeng[1], SHANG Jiacheng[1], HE Haiyan[3], DONG Jiajun[1], CAO Weixue[1*]

1. School of Energy and Safety Engineering, Tianjin Chengjian University, Tianjin 300384, China
2. Tianjin Key Laboratory of Civil Structure Protection and Reinforcement, Tianjin Chengjian University, Tianjin 300384, China
3. Key Laboratory of Solar Energy Utilization and Energy Saving Technology of Zhejiang Province, Zhejiang Energy Group R&D Institute Co., Ltd., Hangzhou 311121, China

Abstract: The transparent envelope structure has huge energy-saving potential, which is the key point to reduce building energy consumption and improve the thermal building environment. The solar radiation transmitted through the transparent envelope structure (transmitted solar radiation) is reflected, scattered and absorbed by the indoor surface, which has a significant impact on the heat gain of the building. In this paper, firstly, the diffuse radiation received by different depths of various indoor surfaces is measured by experimental tests, and the distribution function of transmitted diffuse solar radiation (TDSR) on the indoor surface is established. Secondly, the diffuse solar radiation received by the indoor and outdoor surfaces in different seasons is continuously monitored; the variation of TDSR with time is analyzed, and the distribution function of TDSR on indoor surface with time is proposed. Finally, based on the temporal and spatial distribution characteristics of diffuse radiation under different weather conditions, the variation of TDSR with the weather is studied, and the distribution function of TDSR on the indoor surface with weather changes is established. The distribution function of the TDSR on the indoor surface under different depths, time and weather conditions obtained in this study can supplement and improve the theory of building heat gain and load, and help accurate simulation of building energy consumption.

Keywords: transmitted solar radiation, diffuse radiation, indoor wall surface, distribution characteristics, building heat gain

1. Introduction

Solar radiation has an important influence on building heat gain and indoor thermal environment [1, 2]. Research on the distribution of transmitted solar radiation on indoor wall surfaces is of great significance for optimizing the layout of indoor HVAC systems and human thermal comfort [3]. Lots of scholars are

Special column: Built Thermal Environment GE: YUAN Yanping
Received: Jun 30, 2021
Corresponding author: YAO Wanxiang; E-mail: yaowanxiang@126.com
CAO Weixue cwx@tcu.edu.cn

Nomenclature

a, b, c, d	equation coefficients (dimensionless)	r_d	relative depth (dimensionless)
i_{rtdsr}	relative transmitted diffuse solar radiation (dimensionless)	r_t	relative time sequence number, r_t=time (h)/24 h (dimensionless)
k_t	daily clearness index (dimensionless)		

concerned about the distribution of solar radiation on the indoor wall surface, and according to these research methods and transmission channels, it can be divided into three categories [4–6].

First, solar radiation has been multiple diffuse, reflection, and absorption, and its energy is transmitted and distributed to all of the indoor wall surfaces. This type of research methods can be roughly divided into absorption-reflection-diffuse models and distribution models. The first kind of models consider that the solar radiation incident in the room is absorbed, scattered and reflected by the first wall, and then it is completely scattered after reflected to the second wall. For example, some scholars [4, 7] obtained the distribution law of solar radiation on different regions of the indoor wall by testing and analysis. The second kind of models consider that the transmitted solar radiation is distributed according to the area coefficient, and the distributed solar radiation is absorbed and reflected according to the wall absorptivity, then the reflected solar radiation is redistributed and absorbed after reaching the walls. For example, A.K. Athienitis et al. [8] obtained the distribution coefficient of each wall by comparing the area of each wall and its absorption rate of solar radiation among the walls, and then the incident solar radiation among the walls is distributed according to the distribution coefficient. The third kind of models (e.g. the ASHRAE model) divide the transmitted solar radiation into three parts, that is, reflected back to the outdoors, absorbed by the indoor wall, and dissipated into the indoor air by convective heat transfer [9].

Second, solar radiation is absorbed by the indoor wall and converted into the heat of each wall, which increases the wall temperature and forms a radiation heat transfer network. This type of research method has been carried out by using geometric, numerical and angle coefficient methods [5, 10–12], and an absorption model has been proposed (solar radiation incident to the room is fully absorbed by the first wall surface). K.J. Kontoleon [13, 14] analyzed the radiant heat transfer process, mapped the radiant heat exchange network among indoor walls, and analyzed the distribution pattern of indoor wall radiation for different orientations of glass windows. K. Chatziangelidis et al. [15] proposed a simple distribution factor to distribute the incident global solar radiation in a parallel hexahedral envelope, which takes into account the geometry of the envelope, the perspective coefficient theory and the position of the sun throughout the day. Then an improved method was proposed to calculate the distribution of incident solar radiation over the wall surfaces within a multi-opening enclosed space.

Third, due to the rapid development of simulation technology in recent years, a large number of scholars have applied theoretical methods to simulation software to study the distribution of solar radiation on indoor wall surfaces. Some scholars [16–21] used Monte Carlo models, discrete transfer models, fitness models, heat flow-splitting and artificial neural networks in simulation software to study the distribution of solar radiation on interior wall surfaces. M. Wall [22] compared and analyzed four simulation software (DEROB-LTH, SUNREP (TRNSYS), FRES and tsbi3) using different theoretical models according to the distribution characteristics of solar radiation on the indoor wall surfaces after transmission, and the results showed that there are significant differences in the calculation results of different models.

Based on the summary of the existing research methods and models, this paper collects the diffuse radiation received by various indoor surfaces at different depths through experimental tests, and studies the variations of the transmitted diffuse solar radiation (TDSR) with depth, time and weather. The relevant research results can be applied to the study of human thermal comfort under the influence of solar radiation. At the same time, it is of great significance for building zoning heating and cooling, building shading design and regulation, building energy consumption simulation and load calculation.

2. Materials and Methods

2.1 Experimental tests

2.1.1 Experimental test equipment

In this study, an indoor transmission solar radiation test platform was built, and the main test equipment used was EKO Silicon-based radiation sensor (ML-02). The auxiliary equipment of this experimental test platform includes: experimental test scaffold, data collector (HIOKI-LR8410-30), and data collector expansion board (HOKI-LR8510). The parameters of the main test equipment are shown in Table 1.

Table 1 The parameters of the main test equipment

Equipment	Type	Physical quantity	Measurement range	Response time	Error
EKO Silicon-based radiation sensor	ML-02	solar radiation	0–2000 W/m^2	<1 ms	
Handheld global radiometer	MP-200	solar radiation	0–1999 W/m^2	<1 ms	±5%

2.1.2 Experimental test scheme

(1) Experimental site

In order to prevent the transmitted solar radiation from being blocked by outdoor high-rise buildings or trees, the experimental site should choose a room with no high-rise buildings or trees outside the transparent envelope structure. Therefore, this article chooses the unrestricted room on the 11th floor of Xingzhi Building in the Tianjin Chengjian University, Tianjin, China (39°09′ N, 117°09′ E). The classroom is 3 m high, 3.2 m wide, and 7 m depth. The window is oriented due south. The total floor height of the building is 13 floors, and there are not any high-rise buildings and trees on the outdoor side.

(2) Experimental scheme

The location of the measurement points of the experimental test stand in this study is presented in Fig. 1. Since the closer to the transparent enclosure structure indoors, the greater the change in solar radiation, within 1 m from the transparent enclosure structure, a test position is arranged every 20 cm, and the first test location is close to the transparent enclosure structure, that is, the dotted line 1 in Fig. 1. At this time, the positions of all silicon-based radiation sensors corresponding to the transparent enclosure structure illustrated in Punctuation 1–16 in Fig. 1 are shown. Within the range of 1–2.2 m from the transparent enclosure structure, each test location is separated by 40 cm, and there are three test locations in total. At a distance of greater than 2.2 m from the transparent enclosure structure, each test location is separated by 80 cm until it reaches the opposite wall of the transparent enclosure structure. After the selected experimental test site is arranged as required, there are 12 test locations in total.

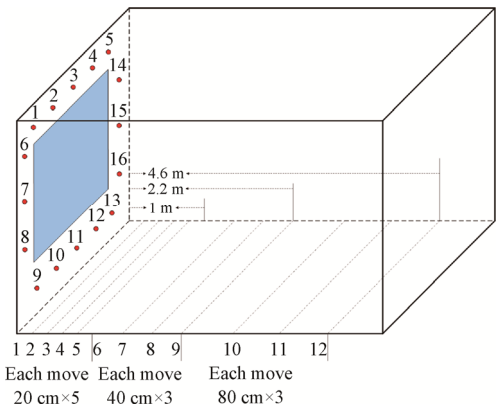

Fig. 1 Layout of measuring points of experimental test support

2.2 Measured data

This experiment was tested in two time periods, the first from September 6th, 2020 to September 17th, 2020 for 11 days and the second from December 2nd, 2020 to December 6th, 2020 for 5 days, with daily tests starting at 8:00 a.m. and ending at 18:00 p.m. Each round of solar radiation was tested at 10 minutes intervals, yielding a total of 1152 valid sets of data.

3. Results and Discussion

3.1 Variation of the distribution of transmitted diffuse radiation on the indoor wall surface with depth

(1) Variation of the distribution of TDSR by the ceiling with depth

First of all, take the indoor ceiling as an example, the distribution of TDSR with the depth of entry at 9:00 a.m., 12:00 a.m. and 15:00 p.m. on the ceiling are shown in Figs. 2–4.

It can be seen from Figs. 2–4 that the closer the distance to the transparent enclosure, the greater the value of TDSR, and as the building depth increases, the value of TDSR gradually decreases. Within 2 m of the transparent enclosure structure, the TDSR decreases most obviously. At 9:00 a.m., 2 m away from the transparent enclosure, the TDSR decreased by nearly 15 W/m^2 and the rate of decrease was 65.2%. At 12:00 p.m., 2 m away from the transparent envelope, the TDSR decreased by nearly 23 W/m^2, with a decrease rate of 54.7%. At 15:00 p.m., 2 m away from the transparent envelope, the TDSR decreased by nearly 18 W/m^2, with a decrease rate of 66.7%. In summary, the decline rate of TDSR at

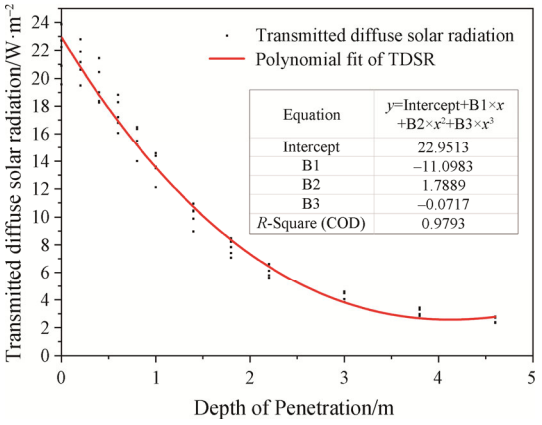

Fig. 2 Distribution of TDSR with depth of penetration at 9:00 a.m. on the ceiling (clear day)

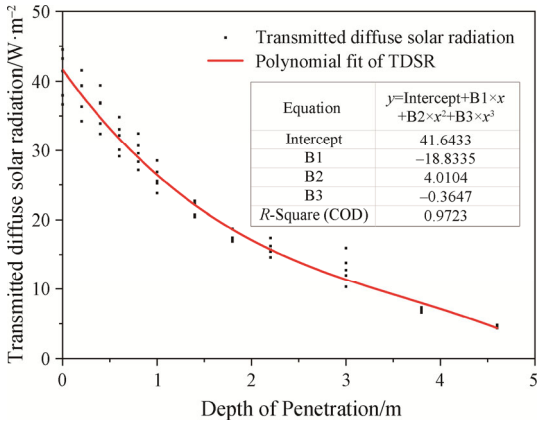

Fig. 3 Distribution of TDSR with depth of penetration at 12:00 p.m. on the ceiling (clear day)

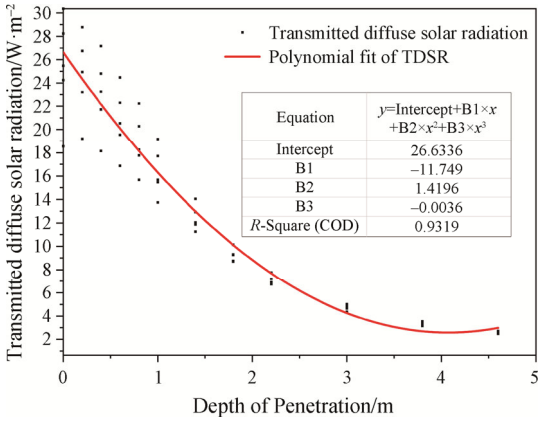

Fig. 4 Distribution of TDSR with depth of penetration at 15:00 p.m. on the ceiling (clear day)

12:00 p.m. on the same day is smaller than that at 9:00 a.m. and 15:00 p.m. Although the solar altitude angle is greater than that of 9:00 a.m. and 15:00 p.m., and the beam solar radiation region is small, but the outdoor solar radiation intensity at noon is greater than that of the morning and afternoon. So the TDSR into the room at noon is higher than that of 9:00 a.m. and 15:00 p.m. Therefore, the decline rate of the TDSR with depth at noon is smaller than that at 9:00 a.m. and 15:00 p.m.

(2) The distribution of TDSR on the floor with depth

Take the floor as an example to analyze the distribution of TDSR with depth. Figs. 5–7 show the distribution of floor TDSR with depth at 9:00 a.m., 12:00 p.m. and 15:00 p.m. on a clear day in autumn.

Since the floor is the main place for people's daily production and life, it is more meaningful to study the distribution of transmitted solar radiation on the floor. It can be seen from Figs. 5–7 that the distribution of TDSR on the floor first reaches the maximum value at a position about 1 m away from the transparent enclosure, and then decreases as the depth increases. The reason is that the TDSR on the floor is significantly blocked by the opaque enclosure under the window. As the depth increases, the shielding effect of the bottom opaque enclosure structure gradually weakens, so the TDSR gradually decreases as the depth increases. The distribution characteristics show different characteristics at different time of the same day. At 9:00 a.m., the TDSR at a depth of 1.5 m showed a

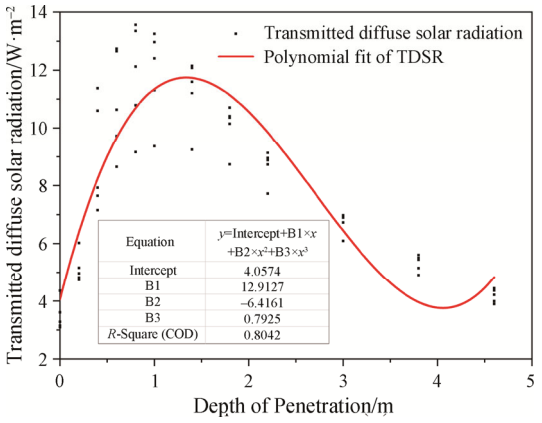

Fig. 5 Distribution of floor TDSR with depth at 9:00 a.m. in autumn (clear day)

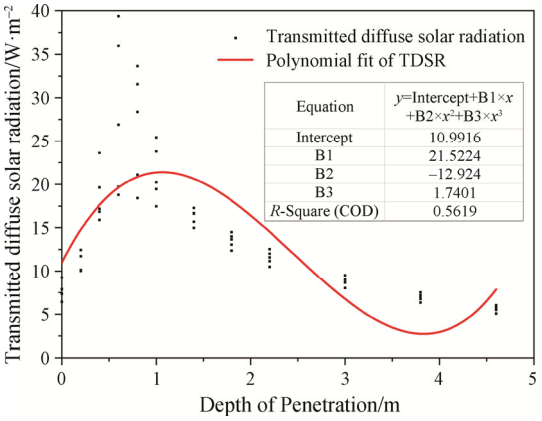

Fig. 6 Distribution of floor TDSR with depth at 12:00 p.m. in autumn (clear day)

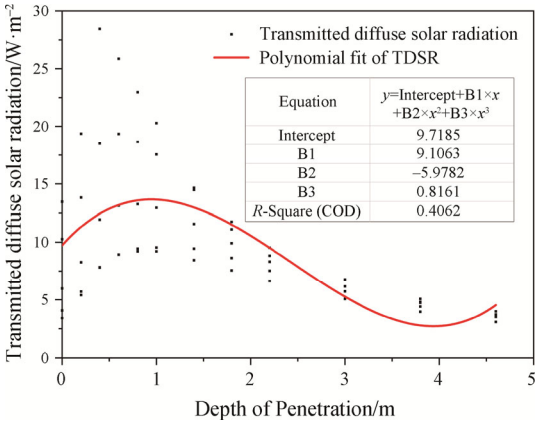

Fig. 7 Distribution of floor TDSR with depth at 15.00 p.m. in autumn (clear day)

maximum value of 12 W/m^2. At 12:00 p.m., TDSR at a position of 1.1 m in depth showed a maximum value of 22 W/m^2. At 15:00 p.m., the maximum value of the TDSR at a depth of 1 m is 13 W/m^2. The peak position of TDSR appears to be different because the solar altitude angle is low in the morning, and the shading effect of the non-transparent enclosure at the bottom of the window is relatively significant, while the solar altitude angle is relatively large at noon and in the afternoon, and the shading effect of the non-transparent enclosure at the bottom of the window is relatively weak.

(3) Variation of the distribution of TDSR on the left wall surface with depth

Fig. 8 shows the TDSR distribution on the left wall at 12:00 a.m. L-1, L-2 and L-3 are the numbers of EKO Silicon-based radiation sensors on the left wall surface from top to bottom, and each sensor is 0.7 m apart. At the test position close to the transparent enclosure, the measured data of L-3 silicon-based radiation sensor is the smallest, followed by the L-1 sensor, and the L-2 sensor is the largest. This is because the L-3 sensor is blocked by the non-transparent enclosure structure at the bottom of the wall where the transparent enclosure structure of the test site is located, so the diffuse radiation intensity of the L-3 sensor is the smallest. However as the depth increases, the shielding effect of the non-transparent enclosure structure at the bottom of the wall where the transparent enclosure structure is located continues to weaken. The diffuse radiation intensity of the L-3 sensor reaches the maximum near the depth of 0.4 m. After that, as the depth increases, the L-3 sensor received by the diffuse radiation gradually decreases. Because the L-1 sensor has the highest position among these three sensors, it is not blocked by the top non-transparent enclosure structure on the wall where the transparent enclosure structure is located at noon, so the diffuse radiation measured by the L-1 sensor is greater than that of the L-2 sensor. Since then, as the depth continues to increase, the diffuse radiation of the L-1 sensor and the L-2 sensor have also continued to weaken.

(4) Variation of the distribution of TDSR on the right wall surface with depth

Fig. 9 shows the distribution of TDSR with depth at 12:00 p.m. on the right wall on a clear day in autumn. R-1, R-2 and R-3 are the numbers of EKO Silicon-based radiation sensors on the right wall surface from top to bottom, and each sensor is 0.7 m apart. It can be seen that at the test position close to the transparent envelope, the TDSR of R-3 sensor is the lowest because it is covered by the non-transparent envelope at the bottom of the wall where the transparent envelope is located, and it increases first and then decreases with the depth. Because of its high height, the diffuse radiation intensity of the R-1 sensor is smaller than that of the R-2 sensor. At 12:00 p.m., the incident direction of the indoor transmitted radiation is due to the south direction, so there is no spot area on the right wall at this time, and thus the attenuation rate of the diffuse radiation intensity of the three sensors with the depth becomes slower, and the maximum value of the diffuse radiation intensity of the R-3 sensor is at the depth of 1 m. At the 9th test position near the depth of 2 m, the diffuse radiation measured by R-1 and R-2 sensors is reduced by 51% and 63% respectively, while the diffuse radiation intensity of R-3 sensor was not in the spot region at this time, but its distance from the spot area was small. Therefore, the diffuse radiation measured by R-3 sensor at this test position is 57% lower than its maximum value.

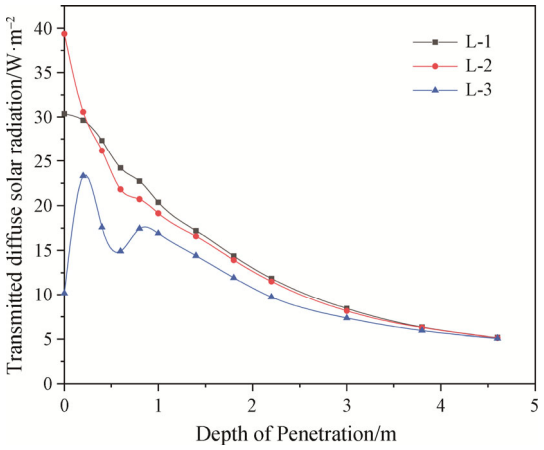

Fig. 8 Distribution of TDSR with depth at 12:00 p.m. on left wall surface in autumn (clear day)

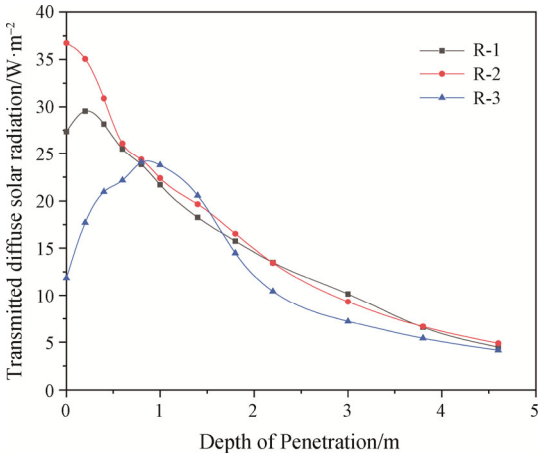

Fig. 9 Distribution of TDSR with depth at 12:00 p.m. on right wall surface in autumn (clear day)

Through the regression analysis of the TDSR on all of the wall surfaces in the room, the dimensionless function relation of the TDSR with depth is obtained. The calculation formula is shown in Eq. (1), and the

Table 2 The coefficients and statistical parameter values of Eq. (1)

Position	Time	Coefficient				*R*
		a	*b*	*c*	*d*	
Ceiling	9:00 a.m.	0.9563	–2.3122	1.8635	–0.3732	0.9793
	12:00 p.m.	0.9254	–2.0926	2.2279	–1.0131	0.9723
	15:00 p.m.	0.7609	–1.6784	1.014	0.0128	0.9319
Floor	9:00 a.m.	0.2898	4.6117	–11.4574	7.0763	0.8042
	12:00 p.m.	0.2748	2.6903	–8.0775	5.5004	0.5619
	15:00 p.m.	0.3351	1.5701	–5.1536	3.5177	0.4062
Left wall surface	12:00 p.m.	06927	–1.3207	0.9613	–0.2091	0.7552
Right wall surface	12:00 p.m.	0.7332	–0.3965	–1.6267	1.4713	0.7939

coefficients and statistical parameter values of Eq. (1) are shown in Table 2.

$$i_{\text{rtdsr}} = a + b \cdot r_d + c \cdot r_d^2 + d \cdot r_d^3 \quad (1)$$

The TDSR distribution of the ceiling position on a clear day is basically not affected by the transmitted beam solar radiation, so the *R* value of the equation is above 0.93. However, the TDSR distribution of the floor position will be affected by the transmitted beam solar radiation, although we have separated the transmitted beam solar radiation from the measured data, but the diffuse radiation of the sunlight direct beam region is still larger than other regions. Its distribution is not uniform, and the *R* value is relatively low, especially at 15:00 p.m. Because the solar altitude angle is relatively lower, the sun moves westward, and there is a part of the location of the TDSR distribution by the opaque envelope structure. Its distribution is more uneven, so the *R* value is relatively lower. Due to the influence of beam solar radiation and the blocking effect of opaque envelope structure, the *R* value of the distribution equation of TDSR distribution on the floor, left and right wall surfaces is relatively low, but this is still a reflection of the distribution equation on the floor, left and right wall surfaces. However, it is still a relatively good method to reflect the distribution pattern of TDSR on the floor, left and right wall surfaces.

3.2 Variation of the distribution of TDSR with time

As showed in Fig. 10, the distribution of TDSR changes with time. In order to explore the variation of the distribution of the TDSR with time, and based on not being obscured by the non-transparent envelope below the window, preventing the test from being affected by doors too close to the rear of the room during the test, the depth of 1 m, 2.2 m and 3.8 m in sunny days in autumn and 1 m, 2.2 m and 3.8 m in sunny days in winter were selected, respectively. It can be seen from Fig. 10, the overall TDSR intensity in winter is higher than that in autumn, because the solar altitude angle is lower in winter, which leads to more diffuse radiation into the

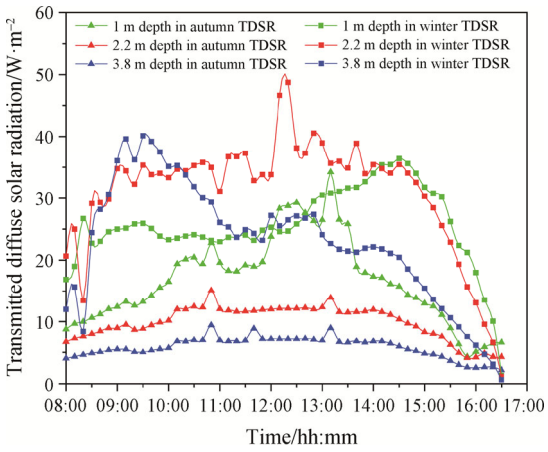

Fig. 10 Variations of TDSR at different depths in winter and autumn with time

room. At 1 m depth, TDSR in autumn presents a hump-shaped distribution, reaching a maximum value of 28 W/m^2 around 12:30 p.m. In winter, the TDSR first increases and then tends to level off with time. It reaches maximum around 14:30 p.m. in the afternoon. The reason is that the solar altitude angle is low in winter, and it is more severely blocked by the opaque envelope structure under the windows. Therefore, it will increase first in the morning. Due to the low solar radiation intensity in winter, the TDSR tends to be smooth in the middle period of time, and finally reaches the maximum at about 14:30 p.m. in the afternoon, and then rapidly declines. The reason is that the solar altitude angle is low and the sunset time is early in winter. Variation of TDSR in autumn at 2.2 m depth tends to level off until about 16:30 p.m. This is because 2.2 m depth is in the middle of the room, the non-transparent envelope below the window does not shade it, and this location does not be directly exposed to the sun due to the high solar altitude angle in autumn, so the change is smooth. In winter, due to the lower solar altitude angle, the lower opaque envelope of the window has a relatively obvious blocking effect on the TDSR, which causes the TDSR at the position of 2.2 m depth to appear certain fluctuations. The maximum

value appears around 12:00 p.m. The TDSR decreases rapidly due to the decrease of the solar altitude angle after 15:00 p.m. At 3.8 m depth, the TDSR changes relatively smoothly in autumn, and the peak of the TDSR in winter appears at around 9:00 a.m., due to the low solar altitude in winter and the location far away from the transparent enclosure. Through regression analysis of the measured values of the TDSR at a depth of 1 m, 2.2 m and 3.8 m indoors in autumn and winter, the corresponding dimensionless function relation formulas are obtained. The calculation formulas are as Eqs. (2)–(7).

The dimensionless equation of the TDSR variation with time at depth of 1 m in autumn is shown in Eq. (2).

$$i_{\text{rtdsr}} = \frac{-6.5118 + 54.153\ 78r_t - 162.2245r_t^2 + 205.3593r_t^3 - 98.4633r_t^4}{1 - 6.2109r_t + 26.9208r_t^2 - 61.1612r_t^3 + 48.9139r_t^4},\ 0 \le r_t \le 1 \tag{2}$$

where r_t is the value obtained by dividing the current time by 24 h.

The dimensionless equation of the TDSR variation with time at the depth of 2.2 m in autumn is shown in Eq. (3).

$$\begin{aligned} i_{\text{rtdsr}} &= 507.4288 - 6412.7613r_t + 33\ 342.799r_t^2 \\ &\quad - 91\ 295.775r_t^3 + 138\ 963.93r_t^4 \\ &\quad - 111\ 538.21r_t^5 + 36\ 883.91r_t^6,\ \ 0 \le r_t \le 1 \end{aligned} \tag{3}$$

The dimensionless equation of the TDSR variation with time at the depth of 3.8 m in autumn is shown in Eq. (4).

$$\begin{aligned} i_{\text{rtdsr}} &= 93\ 568.087 - 194\ 701.92r_t - \frac{26\ 711.777}{r_t} \\ &\quad + 240\ 714.54r_t^2 + \frac{4194.0063}{r_t^2} - 163\ 734.59r_t^3 \\ &\quad - \frac{279.3774}{r_t^3} + 47\ 269.605r_t^4,\ \ 0 \le r_t \le 1 \end{aligned} \tag{4}$$

The dimensionless equation of the TDSR variation with time at the depth of 1 m in winter is shown in Eq. (5).

$$\begin{aligned} i_{\text{rtdsr}} &= -90.8858 + 858.6989r_t - 3098.9212r_t^2 \\ &\quad + 5322.5218r_t^3 - 4275.9125r_t^4 \\ &\quad + 1243.6658r_t^5,\ \ 0 \le r_t \le 1 \end{aligned} \tag{5}$$

The dimensionless equation of the TDSR variation with time at the depth of 2.2 m in winter is shown in Eq. (6).

$$\begin{aligned} i_{\text{rtdsr}} &= -220.7766 + 2561.2516r_t - 12\ 243.347r_t^2 \\ &\quad + 30\ 964.81r_t^3 - 43\ 734.262r_t^4 + 32\ 769.304r_t^5 \\ &\quad - 10\ 207.667r_t^6,\ \ 0 \le r_t \le 1 \end{aligned} \tag{6}$$

The dimensionless equation of the TDSR variation with time at depth of 3.8 m in winter is shown in Eq. (7).

$$\begin{aligned} i_{\text{rtdsr}} &= -68.975 + 113.7254r_t + 2908.3911r_t^2 \\ &\quad - 16\ 279.918r_t^3 + 35\ 649.321r_t^4 - 36\ 024.58r_t^5 \\ &\quad + 13\ 970.391r_t^6,\ \ 0 \le r_t \le 1 \end{aligned} \tag{7}$$

3.3 Variation of the distribution of indoor TDSR with weather

Distribution of indoor TDSR varies with the weather is shown in Fig. 11. Because of the relatively large solar altitude angle during the test, the TDSR at a depth of 1.8 m is less affected by the transmitted beam solar radiation, while this position basically receives no shading effect from the non-transparent envelope, so the TDSR at the indoor depth of 1.8 m on sunny and cloudy days in autumn was selected for analysis. It can be seen from Fig. 11 that the TDSR varies relatively smoothly on a clear day, and its value is smaller than that on a cloudy day. This is because the diffuse radiation in the sky on a clear day is relatively uniform. It will not be affected at 1.8 m depth in autumn. The opaque lower part of the window maintains the blocking effect of the structure. In a cloudy day, due to the randomness of the outdoor sky cloudiness, the TDSR presents a relatively large randomness, and the fluctuation range is relatively large. Take 12:00 p.m. as the boundary, the two sides are symmetrically distributed. At 12:30 p.m., TDSR appears to decline. Because the sky cloud amount is too much, beam radiation is converted to diffuse radiation; diffuse radiation received by the measured region is also blocked by the sky cloud amount, which leads to indoor TDSR decline at this moment.

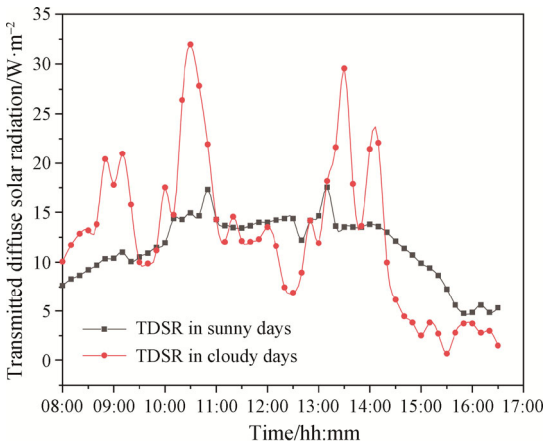

Fig. 11 The distribution of TDSR varies with weather

Through regression analysis of the TDSR in different weather conditions, the corresponding dimensionless function relationship is obtained as Eqs. (8)–(9).

$$\begin{aligned} i_{\mathrm{rtdsr}} &= 614.7516 - 7776.7577 r_t + 40\ 464.257 r_t^2 \\ &\quad -110\ 853.12 r_t^3 + 168\ 776.36 r_t^4 - 135\ 467.41 r_t^5 \\ &\quad + 44\ 788.814 r_t^6, \quad 0 \le r_t \le 1, \quad 0.6 \le k_t \le 1 \end{aligned} \tag{8}$$

$$\begin{aligned} i_{\mathrm{rtdsr}} &= \frac{0.3009 - 2.3058 r_t + 6.5738 r_t^2 - 8.2612 r_t^3 + 3.862 r_t^4}{1 - 7.8592 r_t + 23.0099 r_t^2 - 29.7395 r_t^3 + 14.3204 r_t^4}, \\ &\quad 0 \le r_t \le 1, \ 0 \le k_t \le 0.3 \end{aligned} \tag{9}$$

4. Conclusions

In this article, the indoor TDSR was measured. The different laws of TDSR on the indoor surface with depth, time and weather are studied. The following conclusions can be drawn.

(1) The distribution of TDSR on the floor and ceiling with depth is established (Eq. (1)). The distribution characteristics of TDSR on other surfaces in the room are analyzed.

(2) Taking the indoor depth of 1 m, 2.2 m and 3.8 m in winter and autumn as examples, the indoor TDSR is deeply explored over time. The distribution function of the TDSR with time is constructed (Eqs. (2)–(7)). It is found that the indoor TDSR in winter is higher than that in autumn.

(3) The distribution characteristics of indoor TDSR under different weather conditions are analyzed and its distribution function is constructed (Eqs. (8)–(9)). According to the distribution characteristics of the TDSR, it is found that the indoor TDSR fluctuates greatly on cloudy days, while the indoor TDSR is relatively stable on a sunny day. The study of the distribution characteristics of TDSR on indoor surfaces in this paper is the basis for accurate calculation of transmission solar heat gain in buildings and the relevant conclusions can complement and improve the theory of heat gain and load calculation in buildings.

(4) We have developed models reflecting the distribution law of transmitted TDSR based on experimental tests and theoretical analysis, and adopted a dimensionless approach to minimize the limitation of the equations by geographical location, room geometry, and thermo-physical properties of the indoor surfaces. This approach is general for studying such problems, and the coefficients of the equations can be adjusted according to this approach when developing the models in different locations.

Acknowledges

The authors gratefully acknowledge the support of the National Natural Science Foundation of China (Grant No. 52178083) and Open Project of Key Laboratory of Solar Energy Utilization & Energy Saving Technology of Zhejiang Province (Grant No. JSYJY-KJWZ-2021-011).

References

[1] Benzaama M.H., Menhoudj S., Lekhal M.C., et al., Multi-objective optimisation of a seasonal solar thermal energy storage system combined with an earth – Air heat exchanger for net zero energy building. Solar Energy, 2021, 220: 901–913.

[2] Liu Z., Wu D., Li J., et al., Optimizing building envelope dimensions for passive solar houses in the Qinghai-Tibetan region: Window to wall ratio and depth of sunspace. Journal of Thermal Science, 2019, 28(6): 1115–1128.

[3] Mirzabeigi S., Khalili Nasr B., Mainini A.G., et al., Tailored WBGT as a heat stress index to assess the direct solar radiation effect on indoor thermal comfort. Energy and Buildings, 2021, 242: 110974.

[4] Lee H., Iraqui O., Wang C., The Impact of future fuel consumption on regional air quality in southeast Asia. Scientific Reports, 2019, 9(1): 1–20.

[5] Misiopecki C., Bouquin M., Gustavsen A., et al., Thermal modeling and investigation of the most energy-efficient window position. Energy and Buildings, 2018, 158: 1079–1086.

[6] Omori T., Taniguchi H., Kudo K., Monte Carlo simulation of indoor radiant environment. International Journal for Numerical Methods in Engineering, 1990, 30(4): 615–627.

[7] Zhao Q., Yao W., Zhang C., et al., Study on the influence of fog and haze on solar radiation based on scattering-weakening effect. Renewable Energy, 2019, 134: 178–185.

[8] Athienitis A.K., Stylianou M., Method and global relationship for estimation of transmitted solar energy distribution in passive solar rooms. Energy Sources, 1991, 13(3): 319–336.

[9] Messadi M.T., A theoretical procedure to determine configurations of sunlit room surfaces. ASHRAE Transactions (American Society of Heating, Refrigerating and Air-Conditioning Engineers), United States, 1990. https://www.osti.gov/biblio/5167110

[10] Parameshwaran R., Kalaiselvam S., Harikrishnan S., et al., Sustainable thermal energy storage technologies for buildings: A review. Renewable & Sustainable Energy Reviews, 2012, 16(5): 2394–2433.

[11] Rupp R.F., Vásquez N.G., Lamberts R., A review of human thermal comfort in the built environment. Energy and Buildings, 2015, 105: 178–205.

[12] Liu B.Y.H., Jordan R.C., The long-term average

performance of flat-plate solar-energy collectors. Solar Energy, 1963, 7(2): 53–74.

[13] Kontoleon K., Energy saving assessment in buildings with varying facade orientations and types of glazing systems when exposed to Sun. International Journal of Performability Engineering, 2013, 9(1): 33.

[14] Kontoleon K.J., Glazing solar heat gain analysis and optimization at varying orientations and placements in aspect of distributed radiation at the interior surfaces. Applied Energy, 2015, 144: 152–164.

[15] Chatziangelidis K., Bouris D., Calculation of the distribution of incoming solar radiation in enclosures. Applied Thermal Engineering, 2009, 29(5): 1096–1105.

[16] Pal S., Roy B., Neogi S., Heat transfer modelling on windows and glazing under the exposure of solar radiation. Energy & Buildings, 2009, 41(6): 654–661.

[17] Khatib T., Mohamed A., Sopian K., A review of solar energy modeling techniques. Renewable and Sustainable Energy Reviews, 2012, 16(5): 2864–2869.

[18] Olatomiwa L., Mekhilef S., Shamshirband S., et al., A support vector machine–firefly algorithm-based model for global solar radiation prediction. Solar Energy, 2015, 115: 632–644.

[19] Naeimi H., Kowsary F., An optimized and accurate Monte Carlo method to simulate 3D complex radiative enclosures. International Communications in Heat and Mass Transfer, 2017, 84: 150–157.

[20] Pereira S., Canhoto P., Salgado R., et al., Development of an ANN based corrective algorithm of the operational ECMWF global horizontal irradiation forecasts. Solar Energy, 2019, 185: 387–405.

[21] Teke A., Yildirim H.B., Celik O., Evaluation and performance comparison of different models for the estimation of solar radiation. Renewable & Sustainable Energy Reviews, 2015, 50: 1097–1107.

[22] Wall M., Distribution of solar radiation in glazed spaces and adjacent buildings. A comparison of simulation programs. Energy and Buildings, 1997, 26(2): 129–135.